Buckling of a Pressurized Hemispherical Shell Subjected to a Probing Force

Joel Marthelot
Department of Civil and Environmental Engineering,
Massachusetts Institute of Technology, Cambridge,
MA 02139

Francisco López Jiménez
Ann and H.J. Smead Department of Aerospace
Engineering Sciences,
University of Colorado,
Boulder, CO 80309

Anna Lee
Department of Mechanical Engineering,
Massachusetts Institute of Technology,
Cambridge, MA 02139

John W. Hutchinson
School of Engineering and Applied Sciences,
Harvard University,
Cambridge, MA 02138

Pedro M. Reis
Department of Civil and Environmental Engineering,
Massachusetts Institute of Technology, Cambridge,
MA 02139;
Department of Mechanical Engineering,
Massachusetts Institute of Technology,
Cambridge, MA 02139

Buckling of a Pressurized Hemispherical Shell Subjected to a Probing Force

We study the buckling of hemispherical elastic shells subjected to the combined effect of pressure loading and a probing force. We perform an experimental investigation using thin shells of nearly uniform thickness that are fabricated with a well-controlled geometric imperfection. By systematically varying the indentation displacement and the geometry of the probe, we study the effect that the probe-induced deflections have on the buckling strength of our spherical shells. The experimental results are then compared to finite element simulations, as well as to recent theoretical predictions from the literature. Inspired by a nondestructive technique that was recently proposed to evaluate the stability of elastic shells, we characterize the nonlinear load-deflection mechanical response of the probe for different values of the pressure loading. We demonstrate that this nondestructive method is a successful local way to assess the stability of spherical shells.
[DOI: 10.1115/1.4038063]

1 Introduction

Shell buckling has long been a canonical problem in the structural mechanics community, with a remarkable and longstanding history. As pointed out by Koiter more than fifty years ago [1,2], the critical buckling load of a shell structure is highly sensitive to small imperfections. Indeed, the buckling load, p_{max}, measured in experiments (see Fig. 1 in Ref. [3] for a summary of historical data) can be as low as 20% of the classical prediction for spherical shell buckling derived by Zoelly [4] in 1915

$$p_c = \frac{2E}{\sqrt{3(1-\nu^2)}}\left(\frac{t}{R}\right)^2 \tag{1}$$

where E is the Young's modulus; ν is the Poisson's ratio; and R and t are the radius and thickness, respectively, of the shell. The knockdown factor, $\kappa = p_{max}/p_c$, can then be defined as the ratio between experimental measurements and the classical prediction of the critical buckling pressure. Due to the extreme sensitivity of the buckling pressure to initial imperfections, practical designs of curved shells have traditionally been made using empirical knockdown factors, based on large datasets of buckling experiments [5]. We do not seek here to perform an extensive survey of the vast, technical, and sometimes convoluted prior literature on thin shell buckling. Instead, we direct the interested reader to the recent papers by Hutchinson and Thompson [6,7], where this thematic is covered in detail.

In work of our own [3,8], we have recently demonstrated that the critical buckling load of spherical shells observed in precision experiments can be accurately and deterministically predicted by both finite element modeling (FEM) and a reduced shell theory model. These experiments leveraged a previously developed technique based on a viscous coating mechanism [9] to fabricate thin polymeric shells with significant flexibility and versatility in controlling the underlying parameters. In particular, this experimental protocol yields thin elastic shells of nearly constant thickness, in a rapid, versatile, and precise manner. Moreover, this technique offers the possibility of introducing designed and well-controlled geometric defects that are "*frozen*" at the time of fabrication. By combining experiments with both FEM and a reduced shell theory, we showed that quantitatively predictive relations can be established between the knockdown factor of an elastic shell and the geometry of the defect(s) that it contains. Nonetheless, a detailed a priori knowledge of the geometrical imperfections of the shell is still needed in order to predict the stability of such a structure. In an attempt toward circumnavigating this requirement, a novel nondestructive framework has recently been proposed to probe the stability of uniformly compressed cylindrical shells [10–12] and spherical shells [13]. The basis of this approach is to measure the relationship between the nonlinear deflections of an elastic shell that was initially compressed close to its working load, by subjecting it to a point indentation force, which hereon we shall refer to as *probing force*. The variation of the force measured by the probe with respect to the indentation displacement curve at various levels of compression encodes the characteristics of the stability of the structure.

Here, we study the effect of a probing force applied to a pressurized spherical shell containing a well-defined geometric imperfection. We perform two different sets of experiments, in which the sequential order of the external pressure and the point load probing is reversed. First, we apply a probing displacement and then reduce the pressure within the shell until it buckles. In this case, the indentation induces a local deformation of the shell. By predicting the shell deformation with FEM, we explore the sensitivity of the knockdown factor to different amplitudes of the probe-induced deflection. In the second set of experiments, the sequence is reversed by first reducing the pressure within the shell and then applying a probing displacement until the shell buckles. Naturally, due to the elasticity of the shell, the buckling states of

Contributed by the Applied Mechanics Division of ASME for publication in the Journal of Applied Mechanics. Manuscript received August 31, 2017; final manuscript received September 26, 2017; published online October 19, 2017. Editor: Yonggang Huang.

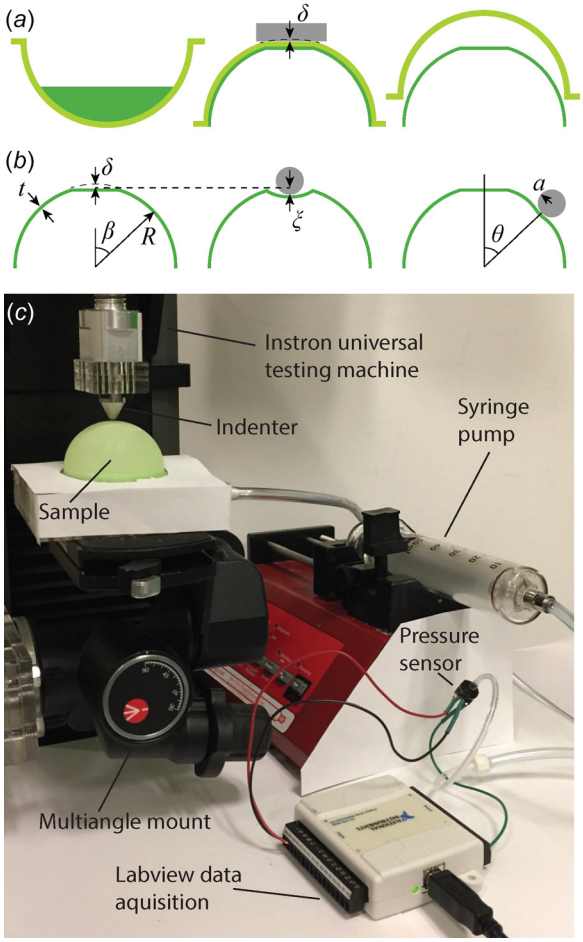

Fig. 1 (*a*) Schematic diagram of the fabrication of a shell with a frozen dimple imperfection with a defect amplitude δ. (*b*) Sketch of the precisely imperfect shell of thickness *t*, characterized by a defect amplitude δ and a defect angle β. The shell is probed by a indenter of radius *a* at an angle θ imposing an additional deflection ξ. (*c*) Photograph of the experimental setup used to measure the pressure variation of a thin hemispherical shells, onto which we impose a set indentation displacement using a universal testing machine (Instron).

the two shells are fundamentally connected, but the two experimental procedures are different and more importantly, as will be seen, a different set of experimental data can be measured in each case.

We also chose to use different types of loading systems for applying the pressure to the shell in the two cases mentioned earlier. When the pressure is applied first, a system was devised to impose a prescribed pressure (pressure control). On the other hand, when the probing force is applied first, the compliance of the system applying the pressure is significantly stiffer such that it is closer to a system with prescribed volume change (volume control). While the advanced post-buckling behavior of the shells under the two types of pressure loading is very different (complete collapse under prescribed pressure and formation of a stable dimple buckle under prescribed volume change), the pressure compliance has very little effect on the buckling condition itself [13–15]. Following the work of Thompson and Hutchinson [13], and supported by our own experiments and FEM simulations, we demonstrate that the combination of pneumatic loading, together with the compressive indentation loading, is a successful local strategy to nondestructively probe the mechanical behavior of the shell. We highlight a parallel effort by Emmanuel Virot, Shmuel M. Rubinstein (Harvard University), Tobias Kreilos and Tobias Schneider on the stability of cylindrical shells set to various levels of axial compression, and probed by a point load to obtain force–displacement curves [12,16]. By contrast, throughout our current study, we shall focus exclusively on hemispherical shells.

Our paper is organized as follows: First, we describe our experimental technique to fabricate thin elastomeric shells containing controlled geometrical imperfections in Sec. 2. We then introduce the methods for our finite element simulations in Sec. 3. In Sec. 4, we measure the buckling strength of the shells under combined pressure loading and a compressive point force. We explore the influence of the geometry of the defects in the shell, as well as the radius of the indenter, on the critical buckling pressure. The mechanical behavior of the shell is then characterized under dead control pressure with a probe under controlled displacement in Sec. 5. Finally, we explore the influence of the angle between the center of the dimple imperfection and the direction of the applied probing force on the stability of the shell in Sec. 6.

2 Experimental Methods

In this section, we detail the rapid prototyping technique used to produce the elastomeric shells and the experimental setup used to fabricate shells with a single dimple-like defect at its pole. We then present the experimental apparatus used to load the hemispherical shell, and describe the protocol followed to measure the critical buckling pressure. The experimental process is outlined in the schematic diagram of Figs. 1(*a*) and 1(*b*). Shells containing one precise frozen defect were produced by coating the inner side of a deformed mold indented by a flat plate (Fig. 1(*a*)). Upon curing, the precisely imperfect thin elastic shell is probed by an indenter and the effect of the probing displacement on the buckling pressure and the nonlinear response of the probe on the initially compressed shell are investigated (Fig. 1(*b*)).

2.1 Fabrication of Shells Containing a Controlled Geometric Defect. The thin elastic shells tested in all of our experiments were fabricated using a previously developed technique [9]. A hemispherical mold (radius $R = 24.85$ mm, machined out of polyacetal through CNC milling) was coated with a silicone-based polymer solution (VPS, Vinylpolysiloxane Elite Double 32, Zhermack, Badia Polesine, Italy). The VPS solution was mixed with a ratio of 1:1 in weight of base to curing agent, for 10 s at 2000 rpm (clockwise), and then 10 s at 2200 rpm (counterclockwise). The drainage flow produces a lubrication film on the mold (Fig. 1(*a*)). Upon curing of the polymer, one obtains an elastic shell of nearly constant thickness ($t = 230$ μm) that can then be readily peeled from the mold. The Young's modulus of cured VPS was measured to be $E = 1.255$ MPa and its Poisson's ratio was assumed to be $\nu = 0.5$.

To fabricate precisely imperfect thin elastic shells (i.e., shells containing a well-defined geometric imperfection), we use a second technique (itself a modification of that of Ref. [9] mentioned earlier), which we had introduced to investigate the effect of the imperfection amplitude on the critical buckling load [3]. We coated the inner side of a thick hemispherical shell of thickness $t_{\text{mold}} = 975$ μm, used as a mold, which was indented by a flat plate attached to a universal testing machine. While holding the indentation constant, the polymer cured inside the deformed mold, thereby imposing an initial defect amplitude, δ, of the imperfect shell (Fig. 1(*a*)). Our previous study [9] showed that this procedure leads to a single dimple-like defect that is localized near the shell pole. In these experiments, to precisely set the initial amplitude of the defect δ, we calibrated the load–displacement relation of the mold and imposed a displacement of the flat plate with the Instron machine until a specific value of the load was reached. The defect amplitude δ was defined as the distance between the position where the plate contacts the mold (characterized by a nonzero value of the load) and the position where the target load was reached. The excess of draining polymer naturally accumulates at the base of the shell, making the hemispherical shell air tight. The shape of the dimple is self-selected by the deformation

of the outer elastic mold under indentation and can be predicted by FEM simulations as described in Ref. [3] and briefly recalled in Sec. 3. Note that in our experiment, the dimple imperfection is always located at the pole of the hemisphere. However, the insensitivity of the dimple location on the critical pressure was recently demonstrated via with nonaxisymmetric numerical analysis [17], which points to the localized nature of the dimple. We do not expect that changing the position of the center of the dimple would affect our results on the buckling process, as long as the dimple is not too near the clamped equator.

2.2 Experimental Apparatus. In Fig. 1, we show a schematic diagram and a photograph of our experimental apparatus. An elastomeric hemispherical shell was mounted onto an acrylic plate and sealed by subsequently injecting a polymer layer through a circular channel in contact with the base of the hemispherical shell such that no residual stresses were imparted onto the shell after clamping its equatorial boundary. The shell was then connected to both a syringe pump (NE-1000, New Era Pump Systems, Inc., Farmingdale, NY) and a pressure sensor (MPXV7002, NXP semiconductors, Eindhoven, The Netherlands). The pressure under the shell was set by extracting a given volume of air with the syringe pump, while simultaneously applying an indentation using an universal testing machine (5943, Instron, Norwood, MA). The acrylic plate was then fixed onto a multi-angle mount [18] (410 Junior Geared Head, Manfrotto, Cassola, Italy). We define the angle θ as the angle between the direction that is perpendicular to the center of the dimple imperfection and the direction of the indentation force (see Fig. 1(*b*)).

The shell was indented at its apex by a rigid spherical Rockwell C diamond indenter (radius $a = 200$ μm, CSM). The force was measured by a universal testing machine (5943, Instron), under imposed displacement conditions. The additional deflection $\xi = w_{pole} - w_0$ corresponds to the variation of the position of the shell apex after and before the application of the load. Following Hutchinson and Thompson [19], we define the dimensionless additional pole deflection by:

$$\bar{\xi} = \sqrt{1-\nu^2}\,\frac{\xi}{t} \tag{2}$$

The point of contact between the probe and the shell corresponds to $\bar{\xi} = 0$. In Secs. 4 and 5, the probe force acts at the center of the dimple imperfection ($\theta = 0$), while nonaxisymmetric cases are explored experimentally in Sec. 6.

In the experiments, we considered four defect amplitudes ($\bar{\delta} = 0.26, 0.40, 0.60, 0.85$), where $\bar{\delta} = \delta/t$ is the defect amplitude normalized by the shell thickness. In Sec. 4, the shells were first probed with an indenter, and then depressurized until buckling occurred. For each shell, we systematically varied the additional pole deflection in the range $0 \le \bar{\xi} \le 15$. While monitoring the internal pressure of the shell, its inner volume was decreased by extracting air at the imposed constant flow rate of 0.1 ml/min, a value that was small enough such that the loading conditions could be considered as quasi-static. The net external pressure acting on the shell is defined as $p > 0$. The shell buckles when the pressure reaches the experimental bucking load $p_{\max}$, defined at the maximum pressure difference between the atmospheric pressure and the internal pressure. All of the experiments were performed with an indenter of radius $a = 200$ μm, with the exception of Sec. 4.3, where the effect of the indenter radius, a, on the knockdown factor is also studied.

For the experiments in Sec. 5, the system was held at a constant level of depressurization p_o, and the shells were then probed with the indenter. The dimensionless pole deflection at which the shell collapses is noted as ξ_0. A reservoir with a large volume of air ($V = 110$ L) was used as a buffer to impose a dead control pressure condition by minimizing the variation of pressure when the indentation was applied. A given volume of air inside the shell was extracted at an imposed constant flow rate of 0.1 ml/min until the pressure reaches p_o a fraction of p_c. The variation of p_o during the indentation phase was kept smaller than 5%, thanks to the large volume of the reservoir. The nonlinear force–displacement curve of the indentation was recorded for a systematic variation of p_o/p_c, between 0 and 0.55. The displacement of the indenter (rigid probe) was controlled and moved at a constant velocity (0.025 mm/s), between $\bar{\xi} = 0$ and 8. The corresponding reaction force, F, was recorded for six independent runs with identical conditions (e.g., the same value of p_o/p_c). The force signal was of the order of a few mN and the experimental noise-to-signal ratio for a single run could be as large as 30%. The irregular fluctuations of the force signal due to the experimental noise tend to cancel out by averaging the six independent, but otherwise identical, runs. After averaging, this experimental noise was reduced to 12%.

3 Simulation Methods

In parallel to the experiments described earlier, we also performed computer simulations using the commercial FEM package ABAQUS/STANDARD. The shells are modeled as hemispheres clamped at the equator. Two different sets of FEM simulations were performed. (i) For a direct comparison with the experimental process, we computed the profile of the imperfect shell under indentation and calculated the buckling load under live pressure. In Secs. 3.1 and 4.1, we model the full fabrication process, mimicking the experimental procedure in FEM. (ii) For a systematic exploration of the effect of the shape of the imperfection on the buckling load, we assumed a generic shape of the dimple. In Secs. 3.2 and 4.2, we study a Gaussian dimple and perform a parametric exploration of the influence of the defect shape on the buckling load. Both set of simulations assume axisymmetry to reduce the computational cost, since it has been shown that nonaxisymmetric bifurcations only take place far into the post-buckling regime [7,20,21].

3.1 Mimicking the Experimental Procedure in the FEM Simulations. In the experiments, the precise shape of the initial dimple is self-selected by the elastic deformations resulting from the fixed indentation of the mold by a rigid plate, at the time of the fabrication process, during curing. In the simulations, to predict the shape of the engineered defect, we used the numerical method that we had developed and experimentally verified previously to study the effect of an imperfection on the critical buckling pressure of the shell [3,8]. The outer elastic mold was modeled as an incompressible Neo-Hookean solid, with reduced hybrid axisymmetric elements CAX4RH, and a thickness $t_{mold} = 975$ μm. The indentation plate was modeled as a rigid flat surface using RAX2 elements. For each defect amplitude δ, the indentation loading of the mold was computed by imposing the vertical displacement of the plate with frictionless contact between the free surfaces. The position of the inner surface of the mold was extracted and assumed to be equal to the outer surface of the fabricated imperfect shell. The defect amplitude of the defect and the corresponding profile computed from FEM had previously been shown to be very close to the shape of the defect extracted experimentally [3]. The imperfection is localized near the pole.

For the current study, after determining the shape of the engineered defect, an additional step was needed to introduce the indentation loading of the shell. This indentation was modeled as an indenter of radius a with frictionless contact between the free surface. Both shell and indenter were modeled again as incompressible Neo-Hookean solid, using reduced hybrid axisymmetric elements CAX4RH. The stiffness of the indenter was taken to be 1000 times that of the shell. The loading was modeled as a live pressure on the outer surface of the structure. Given the unstable post-buckling behavior of the shells, the simulations used the Riks method [22], which simultaneously solves for loads and displacements. This way, the progress of the simulation with the arc length of the load-displacement curve could be measured.

Following the experimental values, the ratio of radius to thickness of the shells studied numerically was varied in the range

$100 \leq R/t \leq 113$. The discretization in the radial direction used 10 elements, and 1000 in the angular direction. These values are chosen according to the convergence analysis performed for previous studies [3,8,23].

Finally, and in order to further emphasize the difference between the effects of an initial geometric imperfection and the indentation, we performed an additional set of simulations in which the deflection due to the indentation was calculated, and applied to the shell as an initial defect, i.e., with no stress. To differentiate this imperfection from the initial dimple present in the simulations with indenters, we refer to it as a *frozen defect*. In this case, an initial simulation is performed to establish the shape under indentation, and this geometry is used to define a new shell, whose buckling load is calculated in a simulation where the only load present is the live pressure.

3.2 Exploration of a Dimple With Generic Shape. After directly contrasting the simulations results to the experiments (results in Sec. 4.1), we then performed a more thorough exploration of the parameters using the simulations alone. For both simplicity and generality, we assumed a simple functional form for the initial shape of the geometric imperfections. The defects were directly introduced in the mesh as a normal displacement of the middle surface, with the profile of a Gaussian dimple

$$w_I = -\delta e^{-(\beta/\beta_0)^2} \tag{3}$$

where β is the angular measure from the pole, and δ and β_0 are parameters that control the depth and angular width of the defect, respectively. The rest of the mesh was then defined assuming constant thickness t perpendicular to the middle surface. To account for the variation of the angular width of the imperfection, β_0, we introduced the geometric parameter following [24]:

$$\lambda = \left\{12(1-\nu^2)\right\}^{1/4} \sqrt{\frac{R}{t}}\beta_0 \tag{4}$$

Our previous results [3,8] confirmed that λ is indeed an appropriate and effective single geometric parameter to characterize how a frozen defect dictates the imperfection sensitivity of our shells. While the Gaussian dimple is only an approximation of the experimental self-selected shape obtained experimentally by indenting the mold with a plate, we find that the best fit to the shape predicted by FEM for the specific mold thickness used in the experiments is obtained with $\beta_0 = 10.8$ deg.

4 Buckling Strength of Hemispherical Shells Under Combined Pneumatic and Point Loading

We start our investigation by following the methodology introduced in Secs. 2.2 and 3.1 to explore and compare the experimental and numerical results. The shells were first probed with an indenter, and then depressurized until buckling occurred. The point force is applied at the apex of the imperfect shell at the location of the largest defect ($\theta = 0$).

4.1 Buckling Strength of Controlled Imperfect Shell Submitted to a Point Force. In Fig. 2, we plot the variation of the knockdown factor κ_d as a function of the dimensionless indentation of the probe $\bar{\xi}$. In the experiments, four shells were fabricated including defects of different amplitudes ($\bar{\delta} = 0.26$, 0.40, 0.60, 0.85). The initial geometric imperfection controls the knockdown factor without indentation, κ_{d0}, and, as long as the exact geometry of the imperfection is appropriately included, can be accurately predicted by simulations and theory [3]. When the shell is indented, we observe three distinct regimes on the knockdown factor with increasing values of $\bar{\xi}$: (i) insensitivity at small values of indentation ($0 < \bar{\xi} \lesssim 1$); (ii) sharp decrease in an intermediate regime

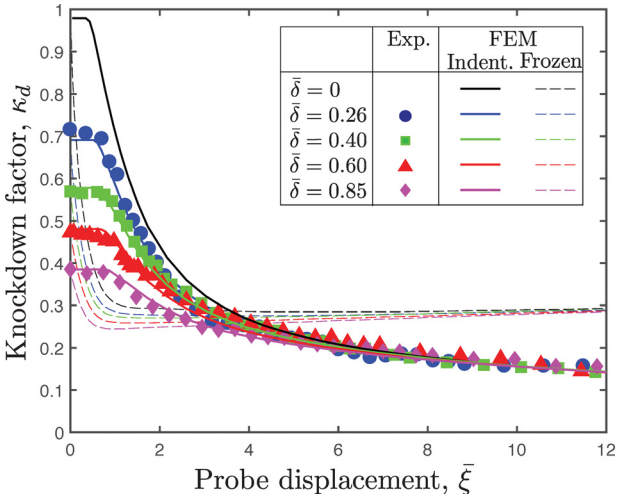

Fig. 2 Knockdown factor, κ_d, versus indentation depth, $\bar{\xi}$. In the experiments (closed symbols), the shells ($R = 24.9$ mm, $t = 220$–250 μm) were fabricated with initial normalized defect amplitude $\bar{\delta} = 0.26, 0.40, 0.60, 0.85$. The solid lines represent simulations by FEM for the corresponding defect profile. The dashed lines are the numerical prediction for a frozen defect with the same geometry.

($1 \lesssim \bar{\xi} \lesssim 5$); and (iii) plateau at large indentation values ($5 \lesssim \bar{\xi} < 15$).

(i) At small indentations ($0 < \bar{\xi} \lesssim 1$), we find that the extent of indentation, $\bar{\xi}$, has no effect on the critical buckling pressure such that $\kappa_d \sim \kappa_{d0}$. The extent of this initial plateau depends on the amplitude of the defect of the shell. Shells including defects with larger amplitudes are less sensitive to small indentations. This effect will be numerically explored in more detail in Sec. 4.2.

(ii) In the intermediate regime ($1 \lesssim \bar{\xi} \lesssim 5$), an indentation $\bar{\xi}$ of up to a few thicknesses translates into a significant drop of the critical buckling load. In this regime, the point load induces a deflection that significantly affects the shape and the amplitude of the initial imperfection. The sharp drop of the knockdown factor with indentation amplitude is a signature of the high sensitivity of the stability of the shell to small probe-induced deflections. This feature is particularly significant for shells that possess a small initial imperfection (e.g., $\bar{\delta} = 0.26$, solid circles in Fig. 2), for which the knockdown factor is decreased to 0.3 κ_{d0}.

(iii) In the limit of large indentation ($5 \lesssim \bar{\xi} < 15$), we observe a lower bound for the knockdown factor. We found that the critical pressure is independent of both the level of indentation and the initial amplitude of the defect. The latter is screened by the deflection of the shell imposed by the indenter. Note that this lower bound is different from the previously studied numerical bound for frozen defects [8] (where the lower bound was shown to depend solely on the shell radius to thickness ratio and the angular width of the frozen defect). This comparison provides evidence for the difference between the cases of direct indentation and the frozen defect, which is further discussed below.

The results from finite element simulations are also plotted in Fig. 2 (solid lines), along with the experimental results, for the same four defect amplitudes of the experiments. The numerical results for the case of a perfect shell without an initial frozen imperfection ($\bar{\delta} = 0$) are also included in the plot, which cannot be compared to experiments because of the inherent small material defects of the shell fabrication process that lead to the unavoidable initial knockdown factor of $\kappa_d \approx 0.75$. Otherwise, there is excellent agreement between experiments and

simulations. Specifically, the FEM data confirm the three regimes described above. This quantitative match further emphasizes the predictive value of our description of the sensitivity of shell buckling to geometric imperfections, which was already observed in our previous study [3], albeit with the frozen imperfections then, as opposed to the combined pressure loading and probing force now. In particular, our current experimental setup is less dependent on the most difficult experimental challenge (the fabrication of the imperfect shells with frozen defect by a small indentation of the mold $\bar{\delta}$) to rely on a much more straightforward deformation process by directly indenting the shell (with comparatively large probe displacement $\bar{\xi}$).

In Fig. 2, the numerical prediction for the direct indentation of the shell (solid line) is also contrasted with the one obtained for the equivalent *frozen defect* with the exact same geometry but no residual stresses (dashed line). The variation of the knockdown factor for the frozen defect is significantly sharper that the one predicted for the direct indentation, which further highlights the difference between frozen geometric imperfections and direct indentation, since the later induces a nonequilibrated stress field in addition to the deflection of the shell.

4.2 Insensitivity of Shell Buckling to the Defect Geometry at Small Indentations. Having experimentally characterized the evolution of the knockdown factor with indentation and validated our numerical method, we now quantify more extensively the effect of the defect geometry on the critical pressure insensitivity within the small indentation; the regime (i) listed in the previous section. We focus on a more generic shape for the dimple, as introduced in Eq. (3). In particular, we focus on the angular width of the defect β_0 on the edge of the plateau, $\bar{\xi}_c$.

In Fig. 3(*a*), we plot the variation of the knockdown factor versus the indentation depth $\bar{\xi}$ for a Gaussian dimple with $\lambda = 3$, indented by a probe of radius $a = 200$ μm. We simulated shells with eleven different initial defects of amplitudes that were distributed in the range $0.05 \leq \bar{\delta} \leq 1$, equally distributed between 0.1 and 1 with incremental steps of $\Delta\bar{\delta} = 0.1$. Again, we recover the three characteristic regimes described in Sec. 4.1. The knockdown factor is first insensitive to the probe displacement (i), then decreases sharply (ii) and, finally, reaches a lower-bound master curve (iii).

From the $\kappa_d(\bar{\xi})$ data in Fig. 3(*a*), we can now define the nondimensional indentation $\bar{\xi}_c$, where the knockdown factor reaches 95% of its value at zero indentation κ_{d0} (highlighted with circles in Fig. 3(*a*)), characterizing the edge of the initial plateau. In Fig. 3(*b*), we plot the variation of $\bar{\xi}_c$ as a function of the amplitude of the initial geometric imperfection, $\bar{\delta}$, for five geometric imperfections, $\lambda = \{2.615, 3, 4, 5, 10\}$. The chosen value of $\lambda = 2.615$ is the critical λ for $\bar{\delta} = 1$, i.e., the geometric parameter that results in the largest reduction of the critical buckling load for an initial defect amplitude of one shell thickness. While a small indentation has an immediate effect on a shell fabricated with a dimple of small amplitude, shells that contain a large initial imperfection are less sensitive to small indentations applied at the position of the defect. Note that under all conditions of indentation, the knockdown factors of shell that present an initial larger defect remain smaller, whatever the value of $\bar{\xi}$. The critical displacement depends strongly on the original defect geometry characterized by λ. Wider initial defects (large value of λ) tend to be more sensitive to small values of the indentation, even with large values of the amplitude of the initial imperfection, $\bar{\delta}$.

4.3 Effect of the Probe Geometry on the Critical Buckling Load. The influence of the probe geometry on the critical buckling load is important for design consideration for real structures in noisy operational environments. In Fig. 4(*a*), we report the variation of the knockdown factor with the probe displacement, for four different indenter geometries (defined by their radius of curvature).The shell used for these experiments had an initial

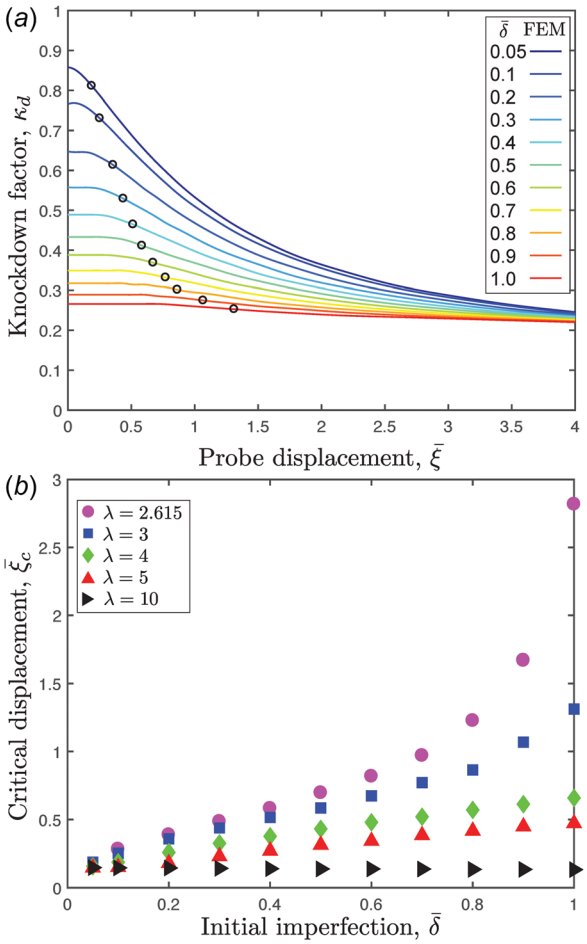

Fig. 3 (*a*) Knockdown factor, κ_d, versus the indentation depth, $\bar{\xi}$, calculated from FEM, for a generic Gaussian dimple with a profile defined by Eq. (3). The radius-to-thickness ratio of the shells is $R/t = 100$, containing Gaussian dimples with $\lambda = 3$ and $\bar{\delta} = [0.05, 0.1, 0.2, \ldots, 0.9, 1]$, distributed between 0.1 and 1 by step of 0.1. (*b*) Critical displacement, $\bar{\xi}_c$, corresponding to a knockdown factor of $0.95\kappa_{d0}$ versus the amplitude of the initial imperfection, $\bar{\delta}$, for shells with $\lambda = [2.615, 3, 4, 5, 10]$ and an indenter radius $a = 200$ μm.

normalized amplitude of $\bar{\delta} = 0.62$. The effect of the shell geometry is rather limited. We observe a slight decrease of the knockdown factor for indenters with a large diameter ($a = 22$ mm and a plate), at large indentation depths ($\bar{\xi} > 3$). Those results are confirmed by the FEM simulations performed for shells containing Gaussian dimples (with $\lambda = 2.615$ and $R/t = 100$), which exhibit a small variation of the knockdown factor with the geometry. The knockdown factors computed with an indenter of radius $a = 0.22$, 2, and 4 mm are identical within 1%. In Fig. 4(*b*), we plot the computed knockdown factor, $\kappa_d(a = 22)$, with an indenter of radius $a = 22$ mm normalized by $\kappa_d(a = 0.22)$ computed with an indenter of radius $a = 0.22$ mm. The maximum effect of the indenter geometry is small, with a maximal decrease of the knockdown factor by 7%, observed for a small initial frozen defect ($\bar{\delta} = 0.05$) and a moderate probe displacement ($\bar{\xi} = 3$).

5 Probing Imperfect Shells Under Dead Pressure

Shifting to the second part of our study, we now focus on an experimental system comprising a shell that is loaded with a constant external pressure (dead control pressure), p_o, as described in Sec. 2.2, earlier. An indentation force, F, is then exerted under imposed displacement, $\bar{\xi}$. In Sec. 5.1, we start by using the indenter as a probe to explore the nonlinear response of the

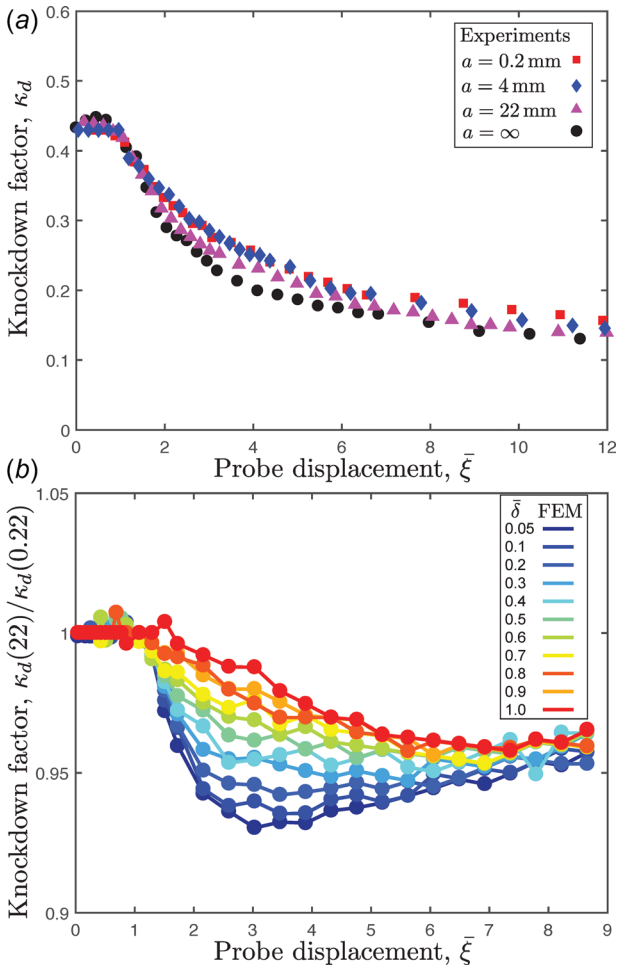

Fig. 4 Experimental knockdown factor, κ_d, versus indentation depth, $\bar{\xi}$, for four geometries of the indenter characterized by their curvature radius (a = [0.2, 4, 22, ∞] mm) for the same shell (R = 24.9 mm, t = 210 μm) fabricated with an initial normalized defect amplitude $\bar{\delta} = 0.62$. (*b*) Knockdown factor, $\kappa_d(a = 22)$, computed by FEM with an indenter of radius a = 22 mm normalized by the knockdown factor, $\kappa_d(a = 0.22)$ computed considering an indenter of radius a = 0.22 mm for a generic Gaussian dimple with a profile defined by Eq. (3). The radius-to-thickness ratio is R/t = 100 and the shells contain Gaussian dimples with $\lambda = 2.615$.

uniformly pressurized shell. We characterize the maximum load, F_{max}, that the shell can carry before buckling occurs, at various levels of depressurization p_o/p_c. In Sec. 5.2, we then compute the work done by the indenter required to reach the buckling state, which corresponds to the energy barrier that the probe must overcome for buckling at the prescribed value of the depressurization. In Sec. 5.3, we show how this quantity can be used as a nondestructive technique to experimentally test the amplitude of the defect and to assess the stability of the shell. We first study a shell that does not contain any engineered defect and is the closest to a perfect shell that we can attain in our experiments (in Secs. 5.1 and 5.2). We then present results for a shell containing a well-defined geometric defect and study its effect on the destabilizing role of the point load (in Sec. 5.3).

5.1 Maximum Carrying Load of a Perfect Shell. In Fig. 5, we plot the measured probe force, $FR/(2\pi D)$, as a function of the deflection imposed by the indenter at the pole of the shell, which is uniformly pressurized. In this plot, the various levels of depressurization, p_o/p_c, are color-coded (see legend); $0 \le p_o$ (Pa) ≤ 66 is

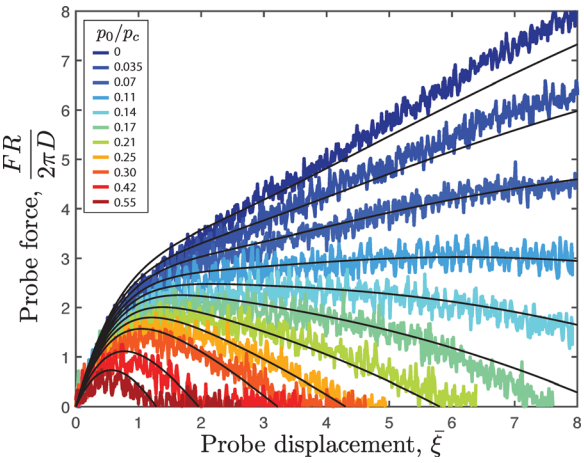

Fig. 5 Normalized probe force, $FR/2\pi D$, versus normalized indentation depth, $\bar{\xi}$, for a shell (R = 24.9 mm, t = 210 μm, $\kappa_{d0} = 0.74$) subjected to 11 prescribed internal pressures. Each curve is the mean of six independent, but otherwise identical, force–displacement curves. Solid lines are predictions from Ref. [13].

varied in steps of ~5 Pa, while the dimensionless probe displacement is imposed in the range $0 \le \bar{\xi} \le 8$.

The passive probing force F has been normalized by the bending rigidity of the shell, $D = Et^3/12(1-\nu^2)$, to read:

$$\bar{F} = \frac{FR}{2\pi D} \tag{5}$$

Obtain the data in Fig. 5, involved averaging the probing force signals for six independent, but otherwise identical, experimental runs at each level of depressurization to increase the experimental signal-to-noise ratio. Note that for large values of the depressurization, the measured forces are close to the limit of the resolution of our force sensor (Instron, 2530-10N) and the signal-to-noise ratio on the force measurement is lower. The test is repeated at 11 different constant levels of external compression p_o normalized by p_c. For $p_o/p_c = 0$ (upper curves of the plot), the indentation process is always stable; the force F increases monotonically, and there are two regimes at small and large indentations. In the limit of small indentation (with respect to the shell thickness, $\xi < t$), the force is described by the linear Reissner's rigidity [18,25,26]. At larger values of the indentation, we observe a nonlinear shell deflection as described by Pogorelov [27,28].

When the level of depressurization of the shell is increased above $p_o/p_c > 0.11$, the load-indentation behavior becomes nonmonotonic and the force plateau reaches a maximum and decreases with increasing probe displacement. For even higher levels of depressurization (when $p_o/p_c \ge 0.21$ within the indentation range spanned experimentally), the force on the probe can eventually reach zero; the shell buckles and snaps dynamically to a collapsed state. This value of p_o/p_c is consistent with the lower bound for the knockdown factor—regime (iii)—described in Sec. 4.1, suggesting that the energy barrier under prescribed pressure or prescribed volume are very similar [29]. Theoretical predictions using small-strain and moderate-rotation theory [1,2,30] were recently derived by Hutchinson and Thompson [13] and Evkin et al. [17,31]. The results from Ref. [13] are computed for the exact condition of depressurization of the shell and superimposed as black lines in Fig. 5. The experimental results are in remarkably good agreement with the theoretical predictions, which is particularly significant since there are no adjustable parameters in the comparison.

We now define the maximum probing force, F_{max}, as a measure of the maximum force that the shell can carry before buckling

occurs, at a set level of depressurization. For an imposed load larger than F_{max}, the shell buckles and snaps catastrophically to a collapsed state. In this section, we test a shell without any engineered defect such that, without indentation, the knockdown factor is $p_{max}/p_c = 0.74$. To extract the maximum force F_{max} for each level of depressurization, the force signal is smoothed with a 50-point moving average filter. In the inset of Fig. 6, we plot a representative example for the average normalized probing force, $\bar{F}$, versus the dimensionless imposed displacement, for $p_o/p_c = 0.21$. The filtered force signal is plotted in red and its maximum indicated with a circle. In Fig. 6, we present the normalized maximum probe force $F_{max}R/2\pi D$ versus the value of the imposed external pressure p_o/p_c, for the same shell. The maximum carrying load of the shell sharply decreases by 70% when p_o/p_c is increased from 0.11 to 0.42. Again, the experimental results are in excellent quantitative agreement with the recent predictions for perfect shells [13], which are also plotted in solid dark line in Fig. 6.

In our experiment, the knockdown factor under pressure alone is $p_{max}/p_c = 0.74$. Note that this value is not unity due to the uncontrollable material imperfections that are intrinsic to the fabrication procedure (e.g., air bubbles in the elastomer, small deviations from sphericity, and small variations in the shell thickness). It is notoriously difficult to fabricate thin shells with larger knockdown factors and, over decades, remarkable experimental efforts were undertaken by Carlson et al. [14] in the 1960 s to fabricate spherical shells by electroforming and chemical polishing treatment, yielding knockdown factors that were, at best, $p_{max}/p_c = 0.86$. The observed knockdown factor value for our shell, $\kappa_d = 0.74$, corresponds to a largest imperfection, $0.15 \leq \bar{\delta} \leq 0.25$, depending on the angular width of the defect [3]. However, the position of the largest imperfection, identified by the position of the dimple without indentation, is not at the pole such that the corresponding values of $\bar{\delta}$ are only an upper bound for the amplitude of the defect at the position of indentation. We observe a deviation at large depressurization where the forces measured experimentally are below the prediction for a perfect shell, which can be attributed to the unavoidable and uncontrollable small imperfections in the structure. In Sec. 5.3, we shall study more systematically the effect of the imperfections on the force–displacement curves.

5.2 Energy Barrier for a Perfect Shell Under Constant Pressure Loading. Under constant pressure loading, there is only one equilibrium point, $\bar{\xi}_0$, at which $F = 0$ for a nonzero indentation and this equilibrium state is unstable. When the indenter reaches $\bar{\xi}_0$, the shell collapses catastrophically. We refer to the work done by the probe to reach this point of buckling as the *energy barrier* that has to be overcome. In this framework, we can compute the area under the force–displacement graph (shaded in gray in the inset of Fig. 6) for each value of depressurization, which is the energy barrier for shell buckling under point loading

$$W = \int_0^{\bar{\xi}_0} F \mathrm{d}\Delta w_{pole} \tag{6}$$

where $\bar{\xi}_0$ is the nontrivial equilibrium point at which the force on the probe reaches zero (circled in the inset of Fig. 6). We recall that, as calculated in Refs. [7,19], the elastic energy in the perfect shell at buckling is $(1/2)p_c\Delta V_c$ where p_c is the critical pressure and ΔV_c is the volume change at the onset of buckling

$$\Delta V_c = 4\pi \frac{(1-\nu)R^2 t}{\sqrt{3(1-\nu^2)}} \tag{7}$$

We normalize the energy barrier for shell buckling by:

$$W_c = \frac{1}{2} p_c \Delta V_c C \frac{t}{R} \tag{8}$$

which is the elastic energy in the perfect shell at buckling with a prefactor where $C = \sqrt{3}/[(1-\nu)\sqrt{1-\nu^2}]$ is a numerical coefficient that only depends on the Poisson's ratio.

In Fig. 7, we plot the energy barrier, W, normalized by W_c, versus the level of depressurization p_o/p_c for all of the force–displacement curves presented in Fig. 5 that reaches $F = 0$ ($p_o/p_c \geq 0.21$). Note that this data (solid circles in Fig. 7) is for a shell without an engineered imperfection (i.e., as "*perfect*" as we can fabricate it in the experiments). Experimentally, we observe that W is close to the normalizing factor W_c for $p_0/p_c = 0.2$. The energy barrier W sharply decreases with increasing depressurization and is as low as 20% of W_c when p_0/p_c reaches 0.3. We then observe a slow decrease of the energy barrier until the buckling pressure is reached. The experimental results are in quantitative

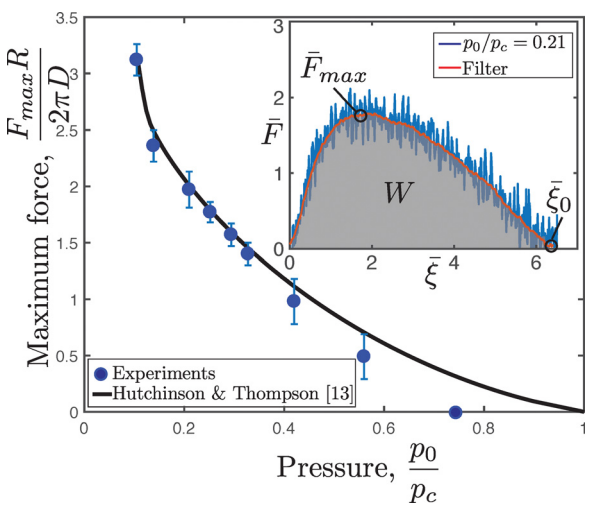

Fig. 6 Normalized maximum probe force, $F_{max}R/2\pi D$, versus prescribed internal pressure normalized by the critical pressure, p_o/p_c, for a shell with $R = 24.9$ mm, $t = 210$ μm, and $\kappa_{d0} = 0.74$. The solid line is a prediction from Ref. [13] for a perfect shell. (Inset) Raw and filtered force signals versus displacement for a shell subjected to an internal pressure $p_o/p_c = 0.21$.

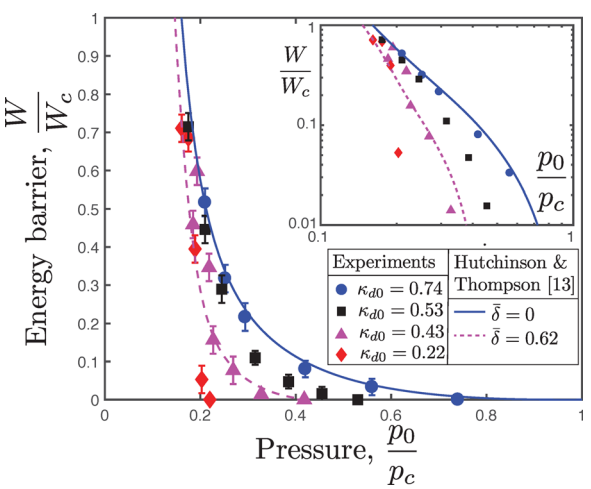

Fig. 7 Normalized energy barrier, W/W_c, versus the normalized internal pressure p_o/p_c for shells with no initial engineered defect ($R = 24.9$ mm, $t = 210$ μm, $\kappa_{d0} = 0.74$, solid circles) and decreasing value of κ_{d0} ($R = 24.9$ mm, $t = 210$–230 μm, $\kappa_{d0} = [0.53, 0.43, 0.22]$). Solid lines are predictions from Ref. [13], for a perfect shell and dashed lines specialized for an initial Gaussian dimple with $\beta_0 = 10.8$ deg and $\bar{\delta} = 0.62$. (Inset) Log–log plot of the same data.

agreement with recent predictions for perfect shells [13] plotted as the solid dark line in Fig. 7. Next, we explore how imperfections result in qualitative changes in the destabilizing role of the point force.

5.3 A Nondestructive Technique to Probe the Shell Defect Experimentally. The same experimental procedure followed in Secs. 5.1 and 5.2 is now repeated for shells containing a dimple-like geometric imperfection of dimensionless amplitude $\bar{\delta}$, which were designed and frozen during fabrication. In Fig. 7, we plot the normalized energy barrier, W/W_c, as a function of normalized pressure, p_o/p_c, for those shells containing a defect. The square, diamond, and triangle data points correspond to shells with dimensionless amplitude $\bar{\delta} = [0.55, 0.62, 1.3]$, respectively. We observe that all shells are stable when $p_o/p_c < 0.18$ (in the range of indentations considered in our experiments) and that the energy barrier decreases sharply just above this threshold, thereby suggesting a universal asymptotic value. The decrease of the energy barrier with pressure is steeper when the amplitude of the imperfection increases. This feature is apparent by plotting the same data in a log–log scale (inset of Fig. 7). Numerical predictions derived from Ref. [13] but specialized for the specific slenderness ($R/t = 120$), material properties ($\nu = 0.5$) and geometry of the experimental dimple shapes, are also plotted in Fig. 7 (dashed line). For these numerical results [13], the shape of the imperfection was approximated and modeled as a Gaussian dimple (see Eq. (3) with $\beta_0 = 10.8$ deg and $\bar{\delta} = 0.62$), as introduced in Sec. 3.2.

As proposed recently [10–12], our results demonstrate that measuring the variation of the energy barrier with the normalized internal pressure can be interpreted as a nondestructive technique to probe the stability of a shell that is uniformly compressed close, but just prior, to its working load. The initial amplitude of the imperfection can therefore be extracted by sequentially increasing the depressurization on the shell and: (i) probing the load-displacement curve (with a minimum threshold slightly larger than zero for the force signal to avoid the catastrophic collapse of the structure); (ii) computing the corresponding energy barrier; and (iii) increasing the depressurization on the shell. The process is iterated until the energy barrier reaches a set small fraction of W_c (for example 5%). The value of the corresponding internal pressure p_o provides information on the initial amplitude of the defect at the position of the probe.

6 Imposing a Nonaxisymmetric Point Load on an Imperfect Shell

So far, we have applied the point load at the same position of the center of the largest frozen defect on the shell (i.e., at the pole, by construction). In this section, we explore the effect of probing away from the polar imperfection. We first focus on the buckling strength of the shell by applying the indentation and then depressurizing the shell until buckling occurs. We then turn to exploring the force–displacement behavior of the probe under a given level of depressurization. The corresponding variation of the energy barrier as a function of the angle at which the point load is applied is crucial to understand the sensitivity of the nondestructive technique described in Sec. 5.3 to probe imperfect shells.

6.1 Influence of Nonaxisymmetry on Knockdown Factor. We now apply an indentation with a nonzero angle, θ, between the apex of the shell (position of the largest defect) and the indentation point (as defined in Fig. 1(*b*)). In Fig. 8(*a*), we plot the knockdown factor κ_d versus the probe displacement $\bar{\xi}$, while varying the orientation angle in the range $0 \le \theta\,(\text{deg}) \le 30$. The circle points correspond to the $\theta = 0$ case that was already studied in Sec. 4.1, for a shell with an initial defect imperfection $\bar{\delta} = 0.62$. For large values of the indentation angles (e.g., $\theta = 30$ deg; squares in Fig. 8(*a*)), we observe two distinct regimes. (I) For small indentation depths ($0 < \bar{\xi} < 2.5$), the buckling process is dominated by the initial imperfection; the shell buckles at the position of the frozen defect at the apex and the knockdown factor is constant and equal to the predicted value for an initial defect imperfection of $\bar{\delta} = 0.62$. (II) For deeper indentations ($2.5 < \bar{\xi} < 15$), the dimple develops at the position of indentation and the knockdown factor decreases with probe displacement.

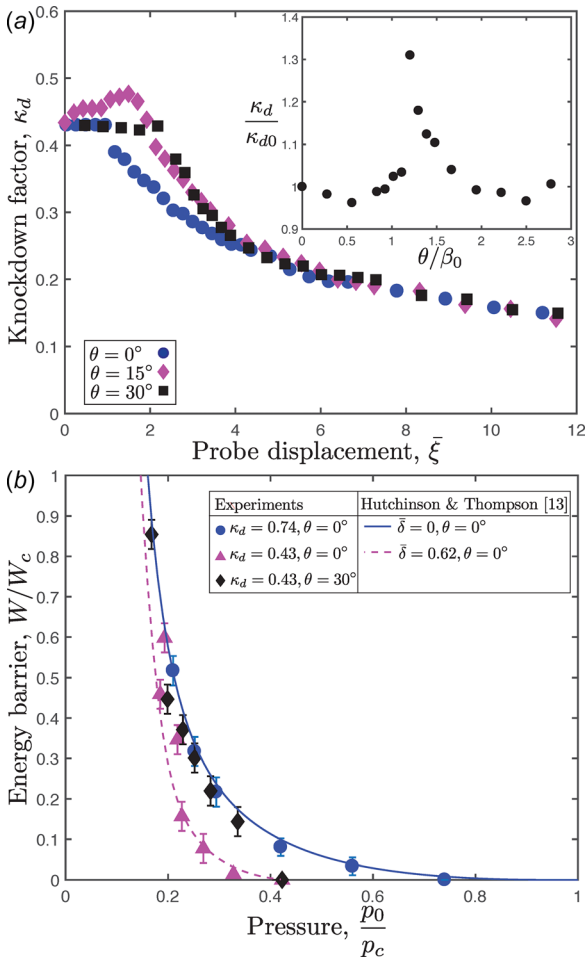

Fig. 8 (*a*) Variation of the knockdown factor, κ_d, versus probe displacement, $\bar{\xi}$, for a shell ($R = 24.9$ mm, $t = 210$ μm) containing an initial an imperfection with $\bar{\delta} = 0.62$. The angle θ is defined between the direction perpendicular to the defect at the shell pole and the direction of indentation. (Inset) Maximum knockdown factor normalized by κ_{d0} versus angle of indentation normalized by the defect angle β_0. (*b*) Variation of the energy barrier with the normalized internal pressure p_o/p_c for two indentation angle θ for the same shell ($R = 24.9$ mm, $t = 210$ μm, $\kappa_{d0} = 0.43$).

Interestingly, for intermediate values of the angle (e.g., $\theta = 15$ deg, diamonds in Fig. 8(*a*)), at small indentations ($0 < \bar{\xi} < 1.7$), we find a surprising increase of the knockdown factor. In this regime, the coupling between the localized deformation associated with the dimple imperfection and the probing force is therefore more subtle. This counterintuitive observation suggests that the indentation of the probe deforms the shell locally in a way that decreases the effect of the dimple imperfection at the pole on the buckling pressure of the shell. This "*healing effect*" of the initial defect has a small but striking effect; an improvement of the initial knockdown factor by approximately 10%, which is remarkable. Still, at larger indentations, the buckling process becomes again dominated by the indentation in a way that screens the initial imperfection. In Fig. 8(*a*) (inset), we report

the relative increase of the maximum knockdown factor versus the angle θ normalized by the defect angle $\beta_0 = 10.8$ deg. The "*healing effect*" is observed when the probe angle is comparable to the initial angle of the defect. The maximum knockdown factor is obtained when $\theta/\beta_0 = 1.2$.

6.2 Influence of Nonaxisymmetry on Energy Barrier. Finally, we repeat the experimental procedure followed in Sec. 5.2 but now with a 30 deg indentation angle, on an imperfect shell (diamonds in Fig. 8(*b*)). For this case (triangles measured at the shell apex), we find no signature of the defect and the energy barrier is similar to the one observed for a shell without an imposed defect (diamonds) until just before the shell buckles when $p_0/p_c = 0.43$. Similar features have been explored numerically, albeit probing the shell way further from the frozen imperfection due to the axisymmetric numerical assumption [29]. The method to test the imperfection is thus local, given the localized nature of the deformation associated with a dimple imperfection, and the interaction between the probing force and the initial dimple at the pole is small. This finding could potentially limit the applicability of the probing technique, because one has to know the position of the largest defect to efficiently test the stability of the shell.

7 Conclusion

We have combined results from experiments, numerical analysis, and reduced shell theory to investigate the buckling of hemispherical shells under combined pressure loading and a compressive point force. First, we explored the sensitivity of the buckling strength of the spherical shells to the probe induced deflection. Second, we demonstrated that by measuring the force displacement of an indenter and probing the shell under various level of depressurization can yield a method to both measure the maximum carrying load of the shell, as well as estimating the energy barrier that has to be overcome for buckling. The passive probing force can be plotted in real time against the displacement. This framework offers a successful nondestructive way to probe the sensitivity of a shell to imperfections, even if the applicability to large-scale structures is still to be demonstrated. In alignment with our previous work [3,8], we have found excellent quantitative agreement between experiments and FEM, as well as experiments and reduced shell theory [6,7].

The excellent agreement that we have found across experiments, FEM and theory calls for future studies on more complex geometries in both experiments and FEM. In particular, a few examples for possible future work include: global defects observed in metal shells and carbon fiber composite shells that are less localized than the frozen dimples of our experiments, defects that point upward (rather than our downward case), or the effect of a dimple located close to the boundary. Other possible directions of considerable interest would be the interaction between multiple well-controlled frozen imperfections, their collaborative effects on the critical pressure and their interactions with a probing force. We hope that the recent resurgence of interest in shell buckling will open new exciting avenues for the rational design of engineered shell structures.

Funding Data

- This work was supported by the National Science Foundation (Grant No. CAREER CMMI-1351449).

References

[1] Koiter, W. T., 1966, "On the Nonlinear Theory of Thin Elastic Shells," Proc., Ser. B, **69**(1), pp. 1–54.
[2] Koiter, W. T., 1967, "General Equations of Elastic Stability for Thin Shells," Symposium on the Theory of Shells to Honor Lloyd Hamilton Donnett, pp. 187–230.
[3] Lee, A., López Jiménez, F., Marthelot, J., Hutchinson, J. W., and Reis, P. M., 2016, "The Geometric Role of Precisely Engineered Imperfections on the Critical Buckling Load of Spherical Elastic Shells," ASME J. Appl. Mech., **83**(11), p. 111005.
[4] Zoelly, R., 1915, "Ueber Ein Knickungsproblem an Der Kugelschale," Ph.D. thesis, ETH Zürich, Zürich, Switzerland.
[5] Samuelson, L. Å., and Eggwertz, S. F., 1992, *Shell Stability Handbook*, Elsevier Applied Science, London.
[6] Thompson, J. M. T., and Van der Heijden, G., 2014, "Quantified 'Shock-Sensitivity' Above the Maxwell Load," Int. J. Bif. Chaos, **24**(3), p. 1430009.
[7] Hutchinson, J. W., 2016, "Buckling of Spherical Shells Revisited," Proc. R. Soc. A, **472**(2195), p. 20160577.
[8] López Jiménez, F., Marthelot, J., Lee, A., Hutchinson, J. W., and Reis, P. M., 2017, "Technical Brief: Knockdown Factor for the Buckling of Spherical Shells Containing Large-Amplitude Geometric Defects," ASME J. Appl. Mech., **84**(3), p. 034501.
[9] Lee, A., Brun, P.-T., Marthelot, J., Balestra, G., Gallaire, F., and Reis, P. M., 2016, "Fabrication of Slender Elastic Shells by the Coating of Curved Surfaces," Nat. Commun., **7**, p. 11155.
[10] Thompson, J. M. T., 2015, "Advances in Shell Buckling: Theory and Experiments," Int. J. Bif. Chaos, **25**(1), p. 1530001.
[11] Thompson, J. M. T., and Sieber, J., 2016, "Shock-Sensitivity in Shell-Like Structures: With Simulations of Spherical Shell Buckling," Int. J. Bif. Chaos, **26**(2), p. 1630003.
[12] Virot, E., Kreilos, T., Schneider, T., and Rubinstein, S., 2017, *Stability Landscape of Shell Buckling* (submitted).
[13] Hutchinson, J. W., and Thompson, J. M. T., 2017, "Nonlinear Buckling Interaction for Spherical Shells Subject to Pressure and Probing Forces," ASME J. Appl. Mech., **84**(6), p. 061001.
[14] Carlson, R. L., Sendelbeck, R. L., and Hoff, N. J., 1967, "Experimental Studies of the Buckling of Complete Spherical Shells," Exp. Mech., **7**(7), pp. 281–288.
[15] Babcock, C. D., 1983, "Shell Stability," ASME J. Appl. Mech., **50**(4b), pp. 935–940.
[16] Kreilos, T., and Schneider, T. M., 2017, "Fully Localized Post-Buckling States of Cylindrical Shells Under Axial Compression," Proc. R. Soc. A, **473**(2205), p. 20170177.
[17] Evkin, A. Y., and Lykhachova, O. V., 2017, "Energy Barrier as a Criterion for Stability Estimation of Spherical Shell Under Uniform External Pressure," Int. J. Solids Struct., **118–119**, pp. 14–23.
[18] Lazarus, A., Florijn, H., and Reis, P., 2012, "Geometry-Induced Rigidity in Nonspherical Pressurized Elastic Shells," Phys. Rev. Lett., **109**(14), p. 144301.
[19] Hutchinson, J. W., and Thompson, J. M. T., 2017, "Nonlinear Buckling Behaviour of Spherical Shells: Barriers and Symmetry-Breaking Dimples," Phil. Trans. R. Soc. A, **375**(2093), p. 20160154.
[20] Nasto, A., Ajdari, A., Lazarus, A., Vaziri, A., and Reis, P. M., 2013, "Localization of Deformation in Thin Shells Under Indentation," Soft Matter, **9**(29), pp. 6796–6803.
[21] Nasto, A., and Reis, P. M., 2014, "Localized Structures in Indented Shells: A Numerical Investigation," ASME J. Appl. Mech., **81**(12), p. 121008.
[22] Riks, E., 1979, "An Incremental Approach to the Solution of Snapping and Buckling Problems," Int. J. Solids Struct., **15**(7), pp. 529–551.
[23] Marthelot, J., Brun, P.-T., López Jiménez, F., and Reis, P. M., 2017, "Reversible Patterning of Spherical Shells Through Constrained Buckling," Phys. Rev. Mater., **1**(2), p. 025601.
[24] Koga, T., and Hoff, N. J., 1969, "The Axisymmetric Buckling of Initially Imperfect Complete Spherical Shells," Int. J. Solids Struct., **5**(7), pp. 679–697.
[25] Reissner, E., 1946, "Stresses and Small Displacements of Shallow Spherical Shells. II," J. Math. Phys., **25**(1–4), pp. 279–300.
[26] Audoly, B., and Pomeau, Y., 2010, *Elasticity and Geometry: From Hair Curls to the Non-Linear Response of Shells*, Oxford University Press, Oxford, UK.
[27] Pogorelov, A. V., 1988, *Bendings of Surfaces and Stability of Shells*, Vol. 72, AMS Bookstore, Providence, RI.
[28] Gomez, M., Moulton, D. E., and Vella, D., 2016, "The Shallow Shell Approach to Pogorelov's Problem and the Breakdown of Mirror Buckling," Proc. R. Soc. A, **472**, p. 20150732.
[29] Hutchinson, J. W., and Thompson, J. M. T., 2017, "Imperfections and Energy Barriers in Shell Buckling," Int. J. Solids Struct. (submitted).
[30] Sanders, J. L., Jr., 1963, "Nonlinear Theories for Thin Shells," Quart. Appl. Math., **21**(1), pp. 21–36.
[31] Evkin, A., Kolesnikov, M., and Prikazchikov, D. A., 2016, "Buckling of a Spherical Shell Under External Pressure and Inward Concentrated Load: Asymptotic Solution," Math. Mech. Solids, **22**(6), pp. 1425–1437.